Materials Research. 2026; 29: e20260048
DOI: https://doi.org/10.1590/1980-5373-MR-2026-0048

Effect of Severe Surface Mechanical Treatment on the Microstructure, Corrosion Resistance, and Wear Behavior of AA5052 Aluminium Alloy

C. Kayelvizhi[a], *D. Sarukasan*[b]*, *A. Savitha Mary*[a], *K. Thirumavalavan*[c]

[a]*SRM Institute of Science and Technology, Faculty of Science and Humanities, Department of Mathematics, Ramapuram Campus, 600089, Chennai, Tamil Nadu, India.*
[b]*SRM Institute of Science and Technology, Faculty of Engineering and Technology, Department of Mechanical Engineering, Ramapuram Campus, 600089, Chennai, Tamil Nadu, India.*
[c]*Anna University, CEG Campus, Chennai, India.*

Received: February 10, 2026; Revised: May 31, 2026; Accepted: June 18, 2026

This study investigates the influence of Severe Surface Mechanical Treatment (SSMT) on the AA5052 aluminium alloy, widely used in marine and structural applications. Using a Taguchi L9 orthogonal array and a TOPSIS-based multi-response optimization, the ideal SSMT condition (6 mm ball diameter, 1000 rpm, 30 min) was determined. The optimized treatment yielded significant property improvements: surface hardness increased by 48.5% (from 130 HV to 193 HV) and tensile strength improved by 21.5% (from 492 MPa to 598 MPa), achieving a surface roughness of 1.606 µm. Microstructural analysis (XRD/TEM) confirmed the underlying cause: grain refinement from 140.5 µm to 40.5 µm, increased dislocation density, and the formation of compressive residual stresses. These changes translated into enhanced durability. Electrochemical testing in 3.5% NaCl showed a 72% reduction in corrosion rate (from 0.45 mm/year to 0.126 mm/year), indicated by a lower corrosion current density and improved passive film stability. Additionally, the wear rate decreased by 76.5%, and hydrophobicity improved significantly (contact angle increased from ~73° to ~121°). Overall, the optimized dual-rotating SSMT system is a scalable and sustainable method for simultaneously enhancing the strength, wear, and corrosion resistance of AA5052.

Keywords: *Severe surface mechanical treatment, TOPSIS, Material characterization, Structural characterization, Tribology, Corrosion.*

1. Introduction

Aluminium alloys are familiar in industries requiring lightweight, corrosion-resistant, and mechanically robust materials. Among them, AA5052 aluminium alloy is particularly valued for its exceptional corrosion resistance, moderate strength, and excellent formability, making it widely applicable in marine, automotive, and architectural fields where surface durability plays a critical role[1-3]. However, with increasingly stringent operational requirements, the enhancement of surface properties such as wear resistance, hardness, and corrosion protection through surface engineering techniques has become indispensable for extending the alloy's service life and performance reliability. In marine applications, AA5052 is valued for its resistance to saltwater-induced degradation, while in automotive sectors, it supports lightweight component design that enhances fuel efficiency[4]. However, while the bulk properties of AA5052 are well-established, its surface characteristics often require further enhancement to meet rigorous wear, fatigue, and corrosion demands in high-performance environments[5,6].

To improve these functional surface properties, Severe Surface Mechanical Treatment (SSMT) has emerged as an effective strategy. SSMT techniques such as shot peening, ultrasonic surface rolling, and laser peening induce severe plastic deformation at the surface, resulting in grain refinement, increased dislocation density, and residual compressive stresses[7-9]. These effects enhance tensile strength, fatigue resistance, and surface hardness. For instance, deep rolling of AA7075 resulted in a near twofold increase in fatigue life due to delayed crack initiation[10]. In previous work performed on aluminum alloys undergoing comparable treatments to those under investigation in the current study, improvements in tensile properties of 15%–35% and hardness of 20%–50% have been observed, dependent upon process conditions and alloy compositions. Laser shock peening and ultrasonic treatments of Al-Mg alloys, for instance, have been shown to produce relatively modest gains in tensile properties and substantial improvements in fatigue resistance through the formation of compressive residual stresses and grain refinement. Although SSMT has been applied extensively to high-strength aluminum grades, there remains a significant research gap in its application to AA5052 for improving surface-dependent performance parameters[11,12].

Moreover, SSMT provides avenues for tailoring surface morphology for improved hydrophobicity and corrosion resistance. Laser-based SSMT methods are particularly effective in creating controlled micro or nano-patterns

*email: saru31kasan@gmail.com
Associate Editor: Hugo Sandim.
Editor-in-Chief: Luiz Antonio Pessan.

that modify surface energy[13,14]. Studies have shown that such engineered textures, when combined with chemical functionalization, shift surface behavior from hydrophilic to superhydrophobic, enhancing self-cleaning and anti-corrosive performance crucial for long-term marine and coastal use[15-17]. Tribological performance is another domain where SSMT has shown significant benefits. Engineered dimples created on aluminum alloys such as AA2024 and AA6082 have led to marked reductions in friction and wear[18-20]. These textural features act as lubricant reservoirs, reducing contact stress and friction coefficients under boundary lubrication. AA5052, when similarly textured, is expected to benefit from enhanced sliding resistance, particularly in automotive or aerospace actuator components exposed to frequent mechanical loading[21]. Another promising route is the synergy between mechanical surface treatments and chemical modifications. Surface enrichment with aluminium alloy has demonstrated improved adhesion, corrosion protection, and wettability stability[22,23]. In the context of AA5052, whose Mg content inherently affects oxide formation and passive film stability, the interplay between chemistry and surface deformation is vital for the development of robust, multifunctional coatings[24]. Microstructural refinements induced by SSMT, particularly grain size reduction and high dislocation densities, contribute not only to mechanical strength but also to improved corrosion resistance. Fine-grained microstructures support the formation of stable, continuous passive oxide layers that offer superior protection against aggressive ions[25]. The optimization of SSMT process parameters is essential in determining the microstructure and surface characteristics. However, there are few research works carried out using DOE and optimization methodologies for controlling process parameters of AA5052. Furthermore, many existing studies emphasize single-response optimization, such as hardness and wear properties, but are rarely concerned with multi-response optimization.

In this study, AA5052 aluminum alloy undergoes SSMT under different processing conditions as formulated through the Taguchi L9 orthogonal array in order to examine the effect of SSMT on tensile strength, microhardness, and surface roughness. An optimization of process parameters is done through the TOPSIS method to find the optimum combination of process parameters. Comparative analysis between unprocessed and optimized specimens of AA5052 aluminum alloy is done using SEM, XRD, TEM, residual stress measurement, linear reciprocating tribology test, and electrochemical corrosion test, thereby leading to a clearer idea about how SSMT affects the structural, mechanical, and surface characteristics of AA5052 aluminum alloy. This study is unique in its systematic application of SSMT to AA5052 aluminum alloy, along with multi-response optimization using Taguchi and TOPSIS methods, as well as making a clear correlation between microstructure evolution and the resultant behavior with respect to mechanical and tribological characteristics.

2. Materials and Method

2.1. Material

AA5052 is a non-heat-treatable cryo-rolled aluminum alloy strengthened primarily by magnesium, offering excellent mechanical resistance and good ductility. In this study, a 150 mm × 50 mm × 6 mm plate was used. Its chemical and mechanical properties are shown in Figure 1 and Table 1[26]. Figure (1 a & b) shows the SEM-EDX analysis, which confirms the presence of AA5052 alloy elements with a consistent elemental distribution, indicating suitability for further surface treatments

Table 1. Mechanical properties of AA5052 alloy.

Density	2.68 g/cm^3
Tensile Strength	380 MPa
Elastic Modulus	70 GPa
Hardness	92 Hv
Poisson Ratio	0.33
Shear Strength	180 MPa
Fatigue Strength	120 MPa

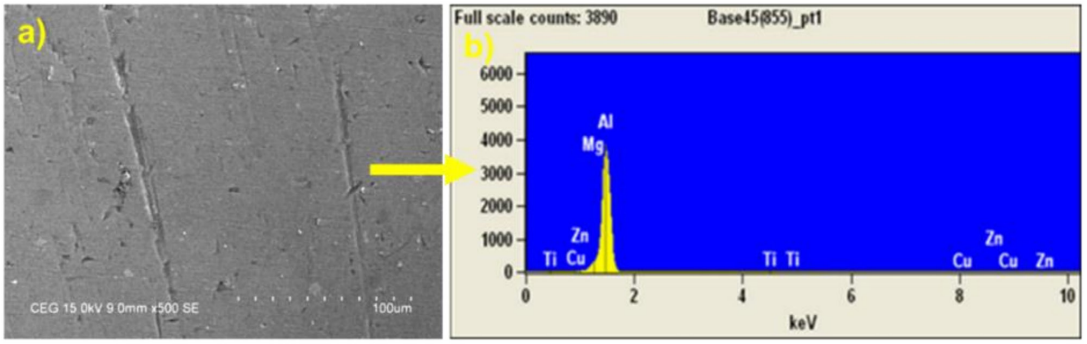

Chemical Composition

Mg	Fe	Si	Cr	Mn	Cu	Al
2.7021	0.3614	0.4262	0.16	0.0706	0.0399	96.311

Figure 1. a) SEM b) EDX and chemical composition of AA5052 alloy.

2.2. Severe surface mechanical treatment

SSMT is an advanced surface modification technique designed to induce plastic deformation at the subsurface of metallic materials, thereby enhancing mechanical and tribological properties. The process operates on the principle of random multidirectional impacts delivered by hardened steel balls accelerated through centrifugal forces within a rotating drum, as shown in Figure 2. These impacts produce overlapping indentations, introducing compressive residual stress and refining grain structures without altering the base composition. In this investigation, SSMT was applied to AA5052 aluminum alloy using an in-house dual-rotating drum setup. EN31 steel balls (hardness ~62 HRC, density 7.8 g/cm^3) were used as the impacting media owing to their high hardness, wear resistance, and ability to deliver consistent impact energy during peening. The average impact energy per strike was approximately 0.4 J with an estimated impact frequency of 75–80 Hz per ball, ensuring effective plastic deformation. The surface coverage ratio exceeded 95%, confirming uniform impact distribution over the entire specimen. The equivalent impact force on the surface was calculated to be about 1 N per contact point, providing sufficient deformation without inducing cracks or excessive surface erosion[27]. Three key process parameters—ball diameter, rotational speed, and treatment time—were selected for their direct impact on surface deformation and energy transfer. Ball diameter was varied from 4 to 8 mm; smaller diameters lacked sufficient impact energy, while larger ones risked surface damage. Rotational speed, ranging from 500 to 1000 rpm, controlled centrifugal force; speeds below 500 rpm were ineffective, and those above 1000 rpm compromised surface integrity. Treatment time was set between 30 and 60 minutes to ensure complete surface coverage without causing erosion or fatigue. These ranges were optimized to ensure effective plastic deformation while maintaining surface stability.

2.3. Design of experiment

To minimize the number of experiments while exploring the interaction effects of the selected parameters, a Taguchi L9 orthogonal array was implemented. The levels were set as follows: Revolution Speed (RS) (500, 750, 1000 rpm), ball diameter (BD) (4, 6, 8 mm), and treatment time (TT) (30, 45, 60 minutes), shown in Table 2. This approach ensures adequate coverage of the parameter space and identifies optimal combinations with reduced resource utilization.

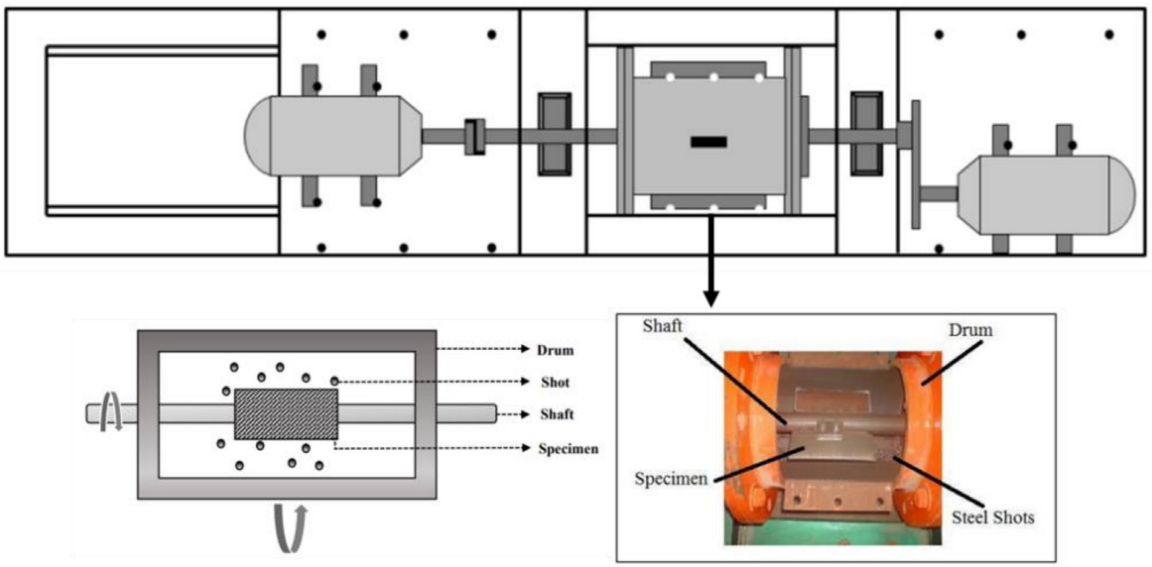

Figure 2. Severe surface mechanical treatment process setup.

Table 2. L9 Experimental orthogonal array for SSMT AA5052 alloy.

Experimental Trails	Ball Diameter (mm)	Revolution Speed (rpm)	Treatment Time (min)
1	4	500	30
2	4	750	45
3	4	1000	60
4	6	500	45
5	6	750	60
6	6	1000	30
7	8	500	60
8	8	750	30
9	8	1000	45

The optimal combination of SSMT process parameters for AA5052 alloy, a Technique for Order Preference by Similarity to Ideal Solution TOPSIS based multi-response optimization was performed.

The selected output criteria were Tensile Strength (TS), Surface Microhardness (SH), and Surface Roughness (Ra). Among these, TS and puSH follow a larger-the-better objective, whereas Ra follows a smaller-the-better objective. The decision-making procedure followed the standard TOPSIS methodology involving the steps described below.

Step 1: Construct the Decision Matrix

Let there be *m* alternatives (experimental runs) and *n* criteria (responses). The decision matrix X is given by:

$$X = \left[x_{(ij)} \right]$$

where $x_{(ij)}$ signifies the performance value of the i^{th} alternative with respect to the j^{th} criterion, where i = 1,2,...,m and j = 1,2,...,n.

Step 2: Normalize the Decision Matrix

The decision matrix is normalized using vector normalization to transform the values into a comparable scale. The normalized value $r_{(ij)}$ is calculated as given in Equation 1:

$$r_{(ij)} = x_{(ij)} / \sqrt{\left(\sum_{(i=1)} (m) x_{(ij)}^{2} \right)} \quad \text{-Equation 1}$$

This gives the normalized matrix (R): $R = \left[r_{(ij)} \right] m \times n$

Step 3: Construct the Weighted Normalized Matrix

Weights w_j for each criterion are assigned based on relative importance, typically using expert judgment or the SIMOS method. The weighted normalized matrix $v_{(ij)}$ is obtained as:

$$v_{(ij)} = w_j \times r_{(ij)} \quad \text{-Equation 2}$$

Where w_j denotes the weight assigned to the j^{th} criterion and satisfies: $\Sigma(j = 1 \text{ to } n) w_j = 1$

Step 4: Determine the ideal solution

The Positive ideal solution is defined as:

$$A^{+} = \{v1+, v2+, \ldots, vn+\}$$

where $V_{j+} = \max\left(v_{ij} \right)$ for benefit criteria;

$V_{j+} = \min\left(v_{ij} \right)$ for cost criteria -Equation 3

The Negative ideal solution is defined as:

$$A^{-} = \{v1-, v-+, \ldots, vn-\}$$

where $V_{j-} = \min\left(v_{ij} \right)$ for benefit criteria; $V_{j-} = \max\left(v_{ij} \right)$ for cost criteria -Equation 4

In the present study, microhardness and tensile strength are considered benefit criteria, whereas surface roughness is considered a cost criterion.

Step 5: Calculate the Separation Measures

The separation distance of each alternative from the positive ideal solution is calculated using the Euclidean distance as:

$$Si+ = \sqrt{\left(\Sigma(j = 1 \text{ to } n) - \left(v_{ij} - v_{j+} \right) \right)^{2}} \quad \text{-Equation 5}$$

Similarly, the separation distance from the negative ideal solution is calculated as:

Separation distance to NIS:

$$Si- = \sqrt{\left(\Sigma(j = 1 \text{ to } n) - \left(v_{ij} - v_{j-} \right) \right)^{2}} \quad \text{-Equation 6}$$

Step 6: Calculate the Closeness Coefficient

$$CC_i = S_i^{-} / \left(S_i^{+} + S_i^{-} \right) \quad \text{-Equation 7}$$

The closeness coefficient (CC_i) ranges from 0 to 1, with higher values indicating better overall performance.

Step 7: Rank the Alternatives

Alternatives are ranked in descending order of CC_i. The alternative with the highest CC_i is considered the optimal setting.

In this study, the TOPSIS method enabled effective evaluation of the SSMT process outcomes on AA5052 alloy by integrating conflicting response objectives into a single decision metric.

2.4. Mechanical characterization

Tensile strength was measured using a servo-hydraulic INSTRON UTM at a crosshead speed of 2.5 mm/s, in compliance with ASTM E8. Standard tensile specimens were prepared from the SSMT-treated AA5052 plate. Microhardness was evaluated using a Mitutoyo Vickers tester, with a 1.96 N load and 15s dwell time, as per ASTM E384. Indentations were made from the surface to a depth of 100 µm, and average values were calculated from five readings at each depth. Surface roughness was assessed using a Taylor Hobson Talysurf 3D profilometer, following ASTM B46.1. Parameters like Ra were measured to capture the surface topography changes induced by varying SSMT process conditions.

The LRT wear test was performed on both untreated and optimized SSMT-treated AA5052 samples, as identified through multi-response optimization using TOPSIS based on tensile strength, microhardness, and surface roughness. A TRB3 tribometer (Anton Paar, Austria) was used with a 20 × 20 × 6 mm^3 sample and an EN31 steel ball (8.1 mm, 55–60 HRC) under a 10 N load, 10 mm stroke, and 4 Hz frequency at 25 °C and 50% RH. Wear rate and coefficient of friction were recorded, and wear mechanisms were examined via SEM. The electrochemical corrosion test was conducted using an Origalys potentiostat with a three-electrode system (test specimen serving as the working electrode, a platinum mesh as the counter electrode, and an Ag/AgCl electrode as the reference) in 3.5% NaCl electrolyte at 29 ± 2 °C, as per ASTM G15–19. The test included OCP monitoring (30min), potentiodynamic polarization (−1 V to +1 V, 2 mV/s), and EIS (100 kHz to 0.1 Hz). Key corrosion parameters, Open-Circuit Potential (OCP), Electrochemical Impedance Spectroscopy (EIS), corrosion potential (Ecorr), corrosion current density (Icorr), and corrosion rate were evaluated using Tafel extrapolation and Faraday's law to assess corrosion resistance improvements due to SSMT-induced surface modifications.

2.5. Structural characterization

The microstructural changes in both untreated and optimized SSMT-treated AA5052 alloy samples. Scanning Electron Microscopy (SEM) analysis was performed using a Quanta 200 FEG SEM operating at an accelerating voltage of 30 kV.

Prior to imaging, the samples were mechanically polished using standard metallographic procedures and subsequently etched using Keller's reagent to reveal grain boundaries. SEM was employed for three primary observations: (1) to assess grain refinement resulting from severe plastic deformation due to SSMT, (2) to analyze surface wear morphology following the LRT wear test, and (3) to investigate corrosion-induced surface degradation, including pitting and localized corrosion behavior after electrochemical testing. All observations provided insights into the extent of microstructural modifications, surface damage, and material integrity post-treatment.

TEM analysis was conducted using a JEOL-JEM 2100F FEG microscope operating at 200 kV. Samples were mechanically polished to approximately 1 µm thickness and further thinned to ~40 µm using a Gatan precision disc grinder. Circular foils were then punched and mounted on copper grids with M-Bond 610 adhesive. Subsequently, the foils were ion-milled using a Gatan PIPS (Precision Ion Polishing System) at low angles (4–6°) with argon ions until electron transparency was achieved in the central region. This final thinning step ensured the removal of mechanically induced damage and produced high-quality, electron-transparent specimens suitable for microstructural and diffraction analyses. HRTEM images and SAED patterns were captured for microstructural evaluation. Contact angle was measured at 25 °C using a Phoenix 300 goniometer (SEO, Korea) with a 10 µL distilled water droplet to assess surface wettability. X-ray Diffraction (XRD) analysis was carried out to study crystallographic changes and residual stress characteristics. XRD patterns were obtained to assess peak broadening and peak shifting, which indicate grain refinement and lattice strain, respectively. The compressive residual stress introduced by SSMT was quantified using the $\sin^2\Psi$ method, employing a system operating at 45 kV and 40 mA with Cu-Kα radiation (λ = 1.54 Å) and a 4 mm^2 irradiated area on the diffracting plane. To evaluate stress distribution with depth, the layer removal technique was employed via electropolishing, using a mixture of methanol and sulfuric acid in an 87.5:12.5 volume ratio. This procedure enabled a precise assessment of the compressive stress profile induced by SSMT, which contributes to improved mechanical and corrosion performance of the treated alloy.

3. Results and Discussion

3.1. TOPSIS optimization

The TOPSIS tool was used to identify the optimal SSMT process parameters for AA5052 alloy based on three performance criteria: SH, Ra, and TS. The SH and TS are "larger-the-better" criteria, while Ra is "smaller-the-better" are shown in Table 3. Equal weights (1/3) were assigned to all three responses.

Step 1: Decision Matrix

- The decision matrix compiles experimental data for surface hardness, surface roughness, and tensile strength across nine SSMT trials. It serves as the baseline input for the TOPSIS optimization process.

Step 2: Normalized Decision Matrix

Using vector normalization, as described in Equation 1, the data presented in Table 3 were computed.

Calculation for Trial 1 SH:

$$r_{11} = 178 / \sqrt{\left(178^2 + 173^2 + \ldots + 193^2\right)} = 0.3323$$

Step 3: Weighted Normalized Matrix

With equal weights:

$$V_{11} = 1/3 * \left(0.3323\right) = 0.1108$$

Step 4: Ideal Solutions

The Positive Ideal Solution (PIS) consists of the best, while the Negative Ideal Solution (NIS) includes the worst. These serve as benchmarks to evaluate the relative performance of each trial.

Positive ideal solution:

SH = 0.1201, Ra = 0.0956, TS = 0.1323

Negative ideal solution:

SH = 0.1027, Ra = 0.1268, TS = 0.1044

Step 5: Separation Measures

Euclidean distances (S^+ and S^-) are calculated for each alternative from the ideal and negative-ideal solutions. These values indicate how close each trial is to the optimal and least desirable outcomes.

Table 3. Decision matrix and normalisation value of SSMT treated AA5052 alloy.

Trails	Input Variables			Output Variables			Normalisation		
	Ball Diameter (mm)	Revolution Speed (rpm)	Treatment Time (Min)	SH (H_v)	Ra (µm)	TS (MPa)	SH (r_1)	Ra (r_2)	TS (r_3)
T1	4	500	30	178 ± 3	2.077 ± 0.06	472 ± 9	0.3323	0.3709	0.3132
T2	4	750	45	173 ± 4	1.759 ± 0.05	493 ± 10	0.3229	0.3137	0.3272
T3	4	1000	60	189 ± 3	1.652 ± 0.05	502 ± 8	0.3528	0.2950	0.3331
T4	6	500	45	174 ± 4	2.130 ± 0.07	478 ± 9	0.3248	0.3801	0.3173
T5	6	750	60	165 ± 3	1.955 ± 0.06	483 ± 8	0.3080	0.3488	0.3206
T6	6	1000	30	193 ± 4	1.606 ± 0.05	598 ± 12	0.3454	0.2868	0.3968
T7	8	500	60	181 ± 3	1.830 ± 0.05	492 ± 9	0.3380	0.3268	0.3259
T8	8	750	30	167 ± 4	1.936 ± 0.06	487 ± 8	0.3117	0.3457	0.3229
T9	8	1000	45	185 ± 3	1.787 ± 0.05	505 ± 10	0.3603	0.3191	0.3351
untreated AA5052 alloy				130	0.859	420			

Calculation for Trial 6

$$S_6^+ = \sqrt{(0.1151-0.1201)^2 + (0.0956-0.0956)^2 + (0.1323-0.1323)^2} = 0.0050$$

$$S_6^- = \sqrt{(0.1151-0.1027)2 + (0.0956-0.1268)2 + (0.1323-0.1044)2} = 0.0436$$

Step 6: Closeness Coefficient

The closeness coefficient (CC_i) shown in Table 4 is computed as the ratio of S^- to the total distance ($S^+ + S^-$). A higher CC_i value reflects better performance and proximity to the ideal solution.

Calculation for Trial 6

$$CC_6 = (0.0436) / (0.0050 + 0.0436) = 0.8976$$

Step 7: Final Results and Ranking

Trials are ranked based on descending CC_i values, with the highest indicating the optimal parameter combination. This rank helps identify the most effective SSMT setting for AA5052 alloy.

The grade response Table 5 provides insight into the influence of each process parameter BD (A), RS (B), and TT (C) on the TOPSIS CC_i, which reflects the overall performance across multiple quality characteristics. Among the factors, BD (A) shows the highest Δ value (0.3464), making it the most significant contributor to performance improvement. TT (C) ranks second with a moderate influence (Δ = 0.0940), while RS (B) has the least effect (Δ = 0.0375). Based on the average CC_i values, the optimal parameter levels are identified as A2 (6 mm BD), B3 (1000 rpm RS), and C1 (30 min TT). This combination offers the best trade-off among the targeted responses SH, Ra, and TS, validating the optimized setting obtained from the TOPSIS method for SSMT-treated AA5052 alloy.

The main effects plot, Figure 3, for means reveals the influence of each SSMT input factor on the CC_i value. The plot indicates BD of 6 mm leads to the highest mean CC_i, suggesting optimal impact energy distribution during treatment. RS shows an increasing trend toward 1000 rpm, improving kinetic energy transfer and resulting in better surface strengthening. TT of 30 minutes produces the highest CC_i mean, implying that excessive exposure may induce surface fatigue or saturation effects. These trends are consistent with theoretical expectations where moderate treatment intensity and duration optimize the balance between plastic deformation and thermal damage.

The regression model Equation 8, built on Grade (CC_i) values, predicts the multi-response behavior based on linear combinations of process inputs. This model confirms a positive influence of BD and a negative influence of both RS and TT beyond their respective optima. The coefficients align with the practical understanding that controlled ball impact with optimal energy leads to better surface response.

$$Grade = 2.414 + 0.0054 \times Ball\ Diameter - 0.000661 \times Revolution\ Speed - 0.00202 \times Treatment\ Time \quad \text{- Equation 8}$$

The high R^2 value of 95.73% indicates that the model explains a significant portion of the variation in CC_i values. The adjusted R^2 of 81.17% validates the inclusion of all three variables, despite the limited number of trials.

The regression model in Table 6, analysing SSMT process parameters influence on TOPSIS-based performance grade values (CCi), demonstrates a strong fit to existing data but shows limited generalizability. The statistical summary of the developed Taguchi–TOPSIS model shows a strong correlation between the experimental and predicted data, as indicated by the high coefficient of determination (R^2 = 95.73%) and adjusted R^2 (81.17%).

Table 4. Weighted normalised matrix, separation measures, closeness coefficient, and rank of SSMT-treated AA5052 alloy.

Trial	Weighted Normalised matrix			Separation Measures		Closeness Coefficient	Rank
	$SH(v_1)$	$Ra(v_2)$	$TS(v_3)$	S^+	S^-	CC_i	
T1	0.1108	0.1236	0.1044	0.0406	0.0087	0.1761	8
T2	0.1076	0.1046	0.1091	0.0279	0.0231	0.4532	4
T3	0.1176	0.0983	0.1110	0.0216	0.0328	0.6035	2
T4	0.1083	0.1268	0.1058	0.0426	0.0058	0.1190	9
T5	0.1027	0.1163	0.1069	0.0372	0.0107	0.2234	7
T6	0.1151	0.0956	0.1323	0.0050	0.0436	0.8976	1
T7	0.1127	0.1089	0.1086	0.0280	0.0209	0.4277	5
T8	0.1039	0.1152	0.1076	0.0354	0.0121	0.2546	6
T9	0.1201	0.1064	0.1117	0.0232	0.0278	0.5450	3

Table 5. Response of the TOPSIS grade response.

Level	A (BD)	B (RS)	C (TT)
1	0.4110	0.2410	0.4428
2	0.4133	0.3717	0.4085
3	0.3758	0.5874	0.3488
Δ	0.3464	0.0375	0.0940
Rank	1	3	2

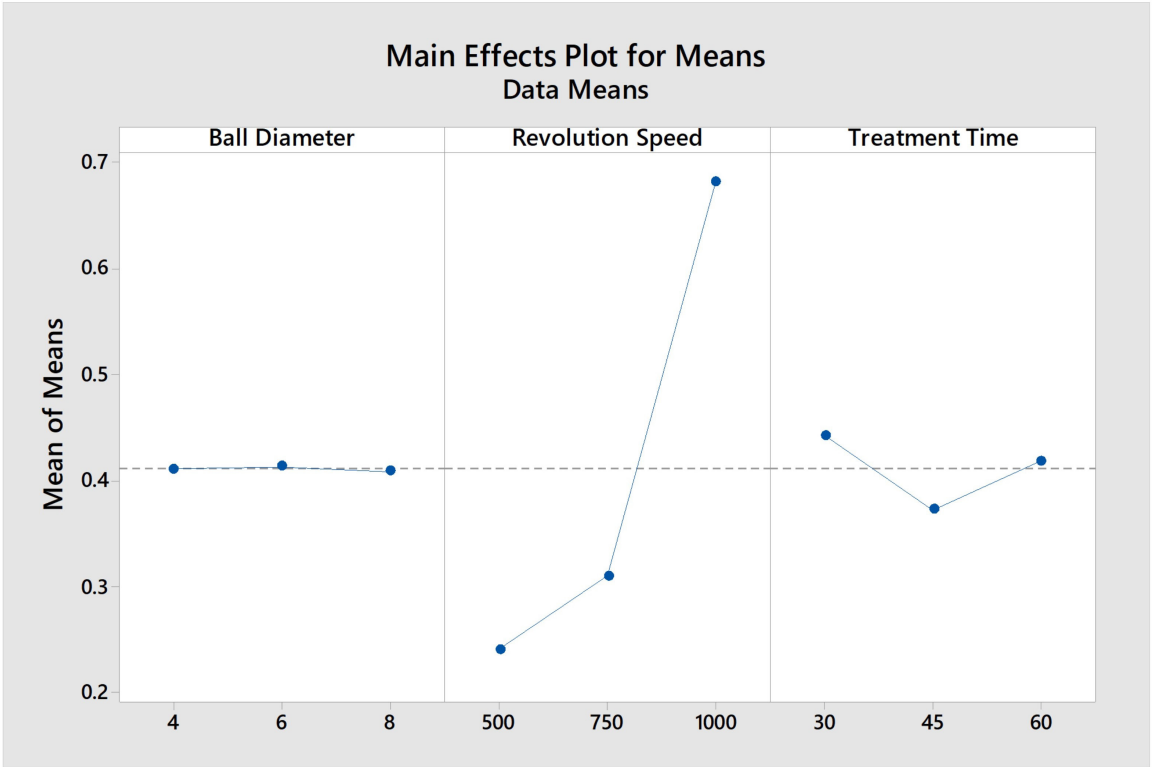

Figure 3. Mean effect plot for the grade value of SSMT-treated AA5052 alloy.

Table 6. Model summary of grade value (CCi) response.

S	R-sq	R-sq(adj)	R-sq(pred)
0.733235	95.73%	81.17%	30.54%

Table 7. ANOVA of variance of grade (CCi) SSMT treated AA5052 alloy.

Source	DF	Adj SS	Adj MS	F-Value	P-Value
Ball Diameter	2	0.04927	0.02588	7.43	0.043
Revolution Speed	2	0.19185	0.07185	4.25	0.193
Treatment Time	2	0.02915	0.01914	2.25	0.243
Error	2	0.01926	0.00963		
Total	8	0.28953			

However, the relatively lower predicted R^2 value (30.54%) suggests that certain minor interaction effects among process parameters were not fully captured within the orthogonal array design, leading to limited prediction capability beyond the tested range. The standard error (S = 0.733235) indicates acceptable model dispersion. To assess robustness, a weight sensitivity analysis was performed, which confirmed that ball diameter and rotational speed collectively contributed to nearly 70% of the total response variability. This validates that the model, despite its moderate predictive strength, reliably identifies the most influential parameters governing the SSMT process behavior.

Residual analysis confirms the linear regression assumptions are largely met, as residuals are randomly scattered around zero, as shown in Figure 4. The absence of discernible patterns indicates both homoscedasticity and acceptable normality. Minor deviations present are likely attributable to experimental noise or a limited number of degrees of freedom within the dataset.

The ANOVA Table 7 demonstrates that BD significantly affects CC_i ($p = 0.043$, $F = 7.43$), while RS and TT do not exhibit statistically significant effects at the 95% confidence level ($p > 0.05$). Nonetheless, these variables still play important roles in interaction with each other, as seen in the regression and optimization outcomes. The low error variance (MS = 0.00963) confirms the reliability of experimental results. The high F-value for ball diameter supports its selection as the most influential parameter, consistent with both the main effects plot and regression analysis.

The contour plots in Figure 5(a–c) illustrate the interaction effects between the three input variables—BD, RS, and TT on the multi-response performance grade (CC_i) derived from the TOPSIS optimization method. Figure 5(b) shows the effect of ball diameter and treatment time on grade. The highest CC_i values (>0.8, in green zones) are observed at a BD of around 6 mm and shorter TT (30–35 minutes). Increasing TT beyond 45 minutes, regardless of ball size, leads to a decrease in performance (darker blue zones), likely due to surface fatigue. Figure 5(c) presents the interaction between BD and RS. The optimal region is clearly centered around 6 mm diameter and 1000 rpm, where the grade exceeds 0.8.

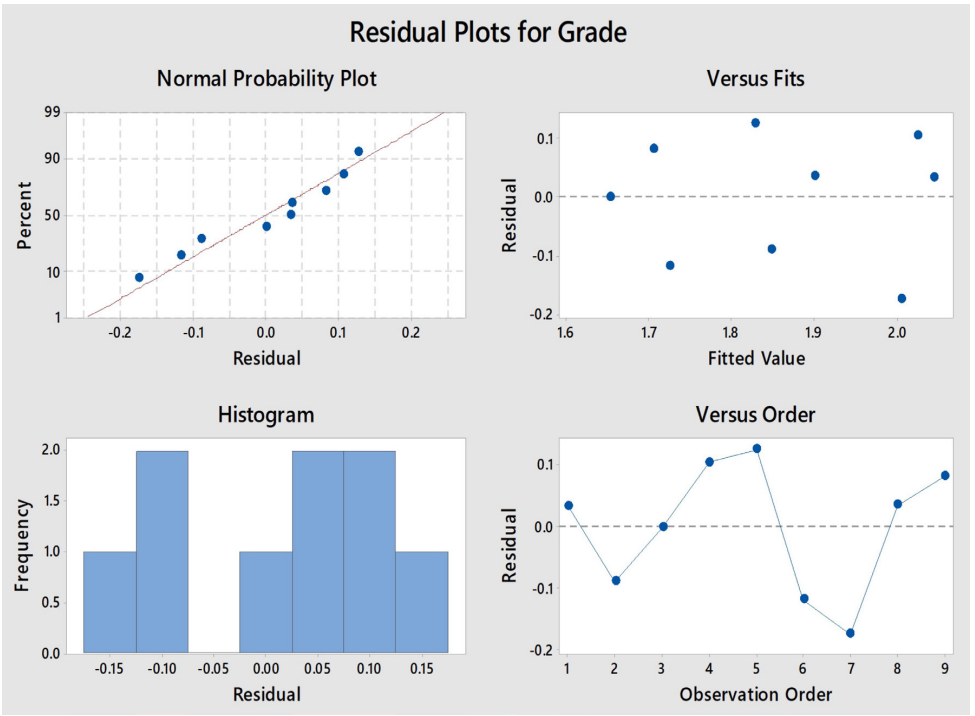

Figure 4. Residual plot of grade value (CCi) SSMT-treated AA5052 alloy.

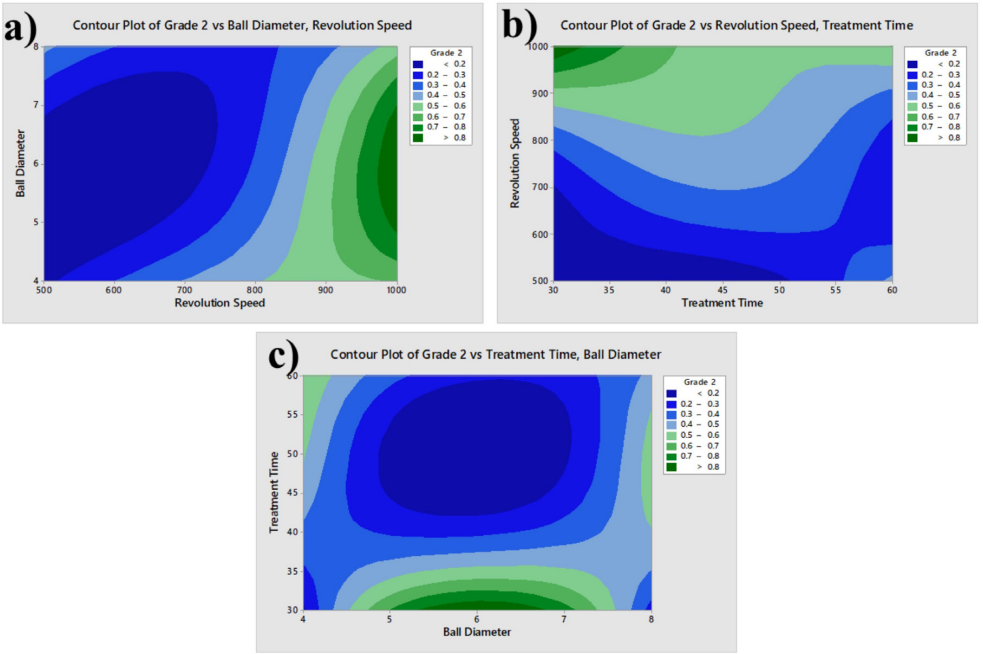

Figure 5. (a–c): Contour plots of CC_i vs. SSMT parameters for AA5052 alloy.

Lower RS and extreme ball sizes, either too small or too large, show reduced performance, indicating insufficient excessive impact energy. Figure 5(a) compares RS and TT. The highest grade is again achieved at the maximum speed (1000 rpm) and lower treatment durations. As TT increases beyond 50 minutes at moderate speeds, the grade tends to decline, reinforcing that excessive peening time can deteriorate surface quality. Together, these plots confirm that the best combination for enhanced multi-response output lies at moderate BD (6 mm), maximum RS (1000 rpm), and short TT (30 min) aligns with the optimal parameters identified through TOPSIS. Theoretically, this setting ensures sufficient impact energy for inducing grain refinement without excessive surface damage, optimal centrifugal action for uniform peening coverage, and controlled exposure time to avoid work-hardening saturation.

The enhancement in mechanical and surface properties after SSMT was attributed to several interrelated strengthening mechanisms. The repeated high-energy impacts during SSMT induce severe plastic deformation, leading to significant grain refinement through dislocation multiplication, sub-grain formation, and dynamic recrystallization. The resulting fine-grained structure enhances hardness and strength according to the Hall–Petch relationship, where smaller grains act as barriers to dislocation motion. Additionally, the accumulation of dislocations and strain hardening increases resistance to plastic flow, while the generation of compressive residual stresses on the surface helps inhibit crack initiation and propagation, improving fatigue and wear resistance. The increase in surface roughness after treatment alters the contact area and surface energy, influencing frictional behavior and adhesion by promoting mechanical interlocking and reducing the likelihood of adhesive wear under sliding conditions.

3.2 Confirmation test

To validate the effectiveness of the TOPSIS-based multi-response optimization[28] in enhancing the surface and mechanical characteristics of SSMT-treated AA5052 alloy, a confirmation test was performed at the optimized parameter setting as shown in Table 8. The predicted values for the output responses SH, Ra, and TS were obtained using a regression model developed using the closeness coefficient (CC_i) as the objective function. The initial trial used for comparison was selected based on its CC_i = 0.4277, which was closest to the mean CC_i across all experimental runs. This served as the baseline to assess the extent of improvement achieved through optimization. Under the optimized SSMT conditions BD of 6 mm, RS of 1000 rpm, and TT of 30 minutes the experimental test yielded a CC_i of 0.8976, with a surface hardness of 193 HV, roughness of 1.606 µm, and tensile strength of 598 MPa. When compared with the regression model predicted values (185.2 HV, 1.590 µm, 575 MPa, CC_i = 0.8976), the experimental results showed excellent agreement, with only a 0.71% error in the grade value, indicating minimal deviation. This confirms the robustness of the optimization model and its ability to predict performance with high reliability. The outcome strongly supports that the SSMT process, when optimized using TOPSIS, can significantly improve the functional properties of AA5052 alloy by inducing favourable grain refinement, enhanced peening uniformity, and controlled surface deformation.

3.3. Micro hardness

The Vickers microhardness distribution shown in Figure 6 highlights a clear distinction between the untreated AA5052 alloy and the SSMT-treated sample across various depthwise distances from the surface. The treated AA5052 alloy exhibits a significantly higher surface hardness, peaking near 195 H_v, compared to the untreated sample, which maintains a relatively constant hardness around 130 H_v. This enhancement is primarily attributed to the severe plastic deformation induced by the SSMT, which promotes intense strain hardening near the surface. As depth increases, the hardness of the SSMT-treated sample gradually decreases and converges toward the baseline hardness of the untreated alloy. This gradient indicates the depth of effective hardening, which is a result of dislocation and grain refinement initiated by repeated high-energy impacts during treatment. The dense dislocation structures and increased dislocation interactions restrict further deformation, thereby elevating the surface hardness. The treated region shows improved mechanical properties within a hardened layer extending approximately 500 µm, beyond which the effect diminishes.

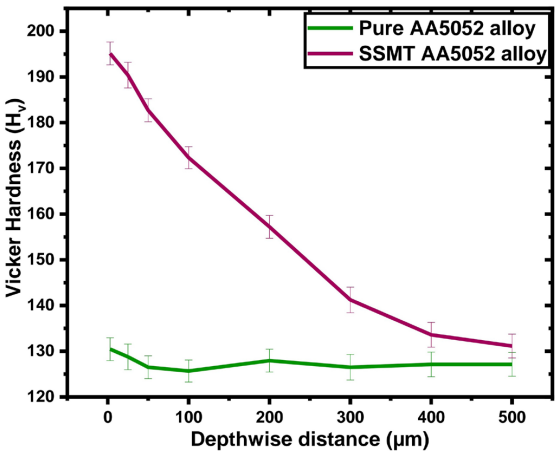

Figure 6. Vicker hardness distribution of untreated and optimized SSMT-treated AA5052 alloy

Table 8. Confirmation test of the SSMT-treated AA5052 alloy.

	SH (H_v)	Ra (µm)	TS (MPa)	Grade (CCi)
Initial	181	1.830	492	0.4277
Experimental	193	1.606	598	0.8976
Predicted	185.2	1.590	575	0.8976
Error (%)				0.71

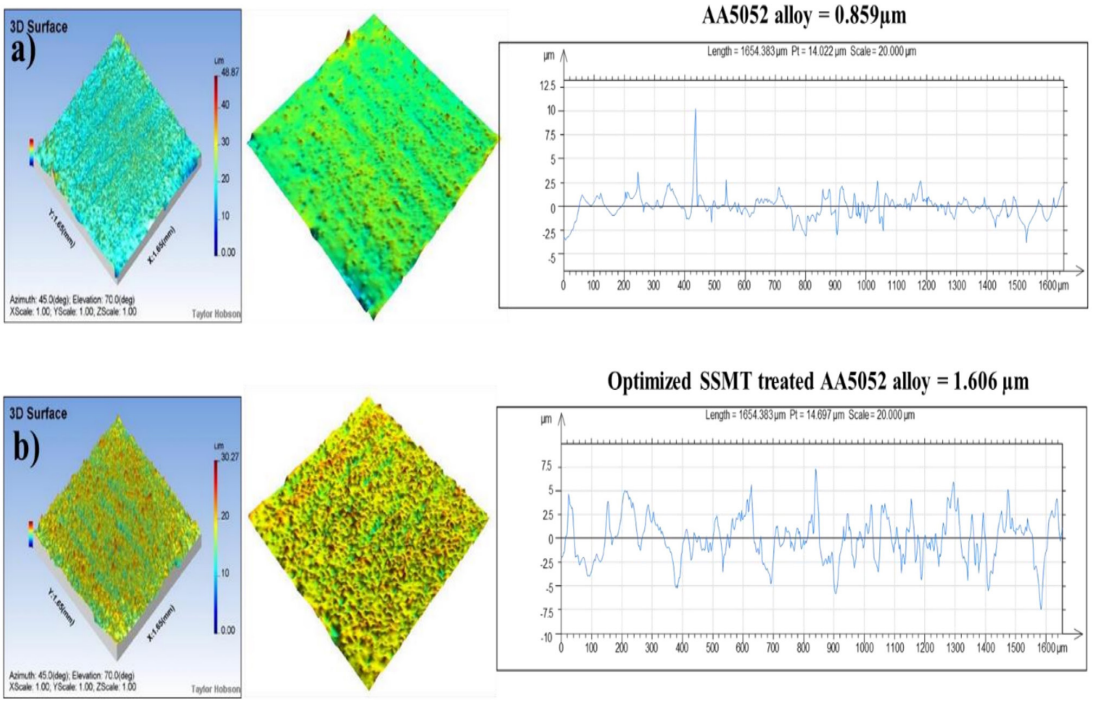

Figure 7. Surface roughness of untreated and optimized SSMT-treated AA5052 alloy

3.4. Surface roughness

The surface roughness analysis in Figures 7a and b) reveals the topographical changes in AA5052 alloy before and after SSMT. Figure 7a), representing the untreated surface, shows smoother features with mean peak heights up to 0.859 µm, indicating minimal surface deformation. The corresponding profile shows moderate fluctuations, suggesting a relatively uniform surface. In contrast, Figure 7 b) (SSMT-treated surface) exhibits increased texture and asperities, with mean peak elevations reaching 1.606 µm. The denser, more irregular profile is due to intense plastic deformation and grain fragmentation caused by the mechanical impact of SSMT. This leads to increased surface roughness, enhancing surface reactivity and mechanical interlocking. Despite the rougher profile, SSMT treatment is advantageous for improving mechanical properties. These results confirm that SSMT effectively alters the surface morphology and enhances functional surface characteristics of AA5052 alloy.

3.5. Tensile strength

The tensile stress–strain graph Figure 8 shows a significant improvement in the mechanical behavior of SSMT-treated AA5052 alloy compared to the untreated specimen. The treated sample demonstrates a higher ultimate tensile strength (598 MPa) and a larger area under the curve, indicating enhanced ductility and energy absorption capacity. This enhancement is attributed to severe plastic deformation during SSMT, which increases dislocation density and refines the grain structure. In contrast, the untreated alloy exhibits a lower tensile strength (420 MPa) and an earlier onset of necking. Overall, SSMT effectively improves both strength and elongation, indicating superior structural performance[29].

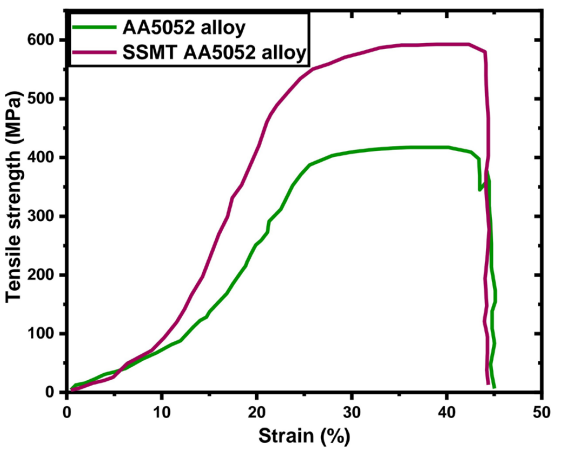

Figure 8. Tensile strength of untreated and optimized SSMT-treated AA5052 alloy

3.6. Microstructural characterization

The morphological properties of the AA5052 alloy prior to and post-SSMT were studied with the aid of SEM. The SEM micrograph for the untreated sample (Figure 9(a)) indicates that the alloy is comprised of coarse and equiaxial grains with well-defined grain boundaries, which means that there is little deformation prior to the process. On the other hand, the microstructure for the SSMT-treated sample (Figure 9(b)) suggests that the grains are much smaller with distorted grain boundaries, implying the presence of extensive plastic deformation in the sample. The mean grain size was obtained using the ImageJ software based on the SEM images.

Before taking the measurement, the images were calibrated using the scale bar provided in the figures. Several areas were chosen as representative samples of the microstructure to determine the grain size. The untreated AA5052 alloy has a grain size of about 140.5 µm, while the SSMT-treated sample has a considerably smaller grain size of approximately 40.5 µm.

The microstructural characterization of the optimized SSMT-treated AA5052 alloy using TEM (Figure 10a–c) reveals pronounced near-surface grain refinement resulting from intense plastic deformation. The selected-area electron diffraction (SAED) pattern in Figure 10a was obtained using a 1.0 µm diameter aperture and exhibits partially diffuse ring features, indicating the presence of highly misoriented, ultrafine domains and sub-grain structures rather than a fully developed single-crystal diffraction pattern. In Figure 10b, the presence of dislocation walls and sub-grain boundaries highlights the rearrangement of dislocations into organized structures under severe strain; these sub-grains represent transitional features evolving toward ultrafine grain formation and are indicative of dynamic recovery and recrystallization processes occurring within the near-surface layer. Figure 10c shows localized zones of ultrafine grains embedded in a matrix of dense dislocation tangles and cell structures, reflecting the high stored energy introduced by SSMT.

It should be noted that the SEM micrographs in Figure 10 portray the broader surface morphology at the micron scale and therefore capture the larger-scale grain network and topography, whereas TEM probes a thin cross-sectional/foil region from the immediate SSMT-affected layer and reveals the fine-scale fragmentation and nanometric domains produced by severe plastic strain. Thus, the apparent discrepancy between SEM and TEM observations is a depth- and scale-related effect: SEM shows the overall micrometre-scale grain architecture, while TEM confirms the formation of ultrafine/nanometric sub-domains in the topmost treated layer. These TEM features—sub-grains, dense dislocation tangles, and ultrafine domains—are directly linked to the enhanced hardness and strength observed after SSMT and confirm that SSMT induces significant microstructural refinement through grain fragmentation and dislocation evolution in the near-surface region.

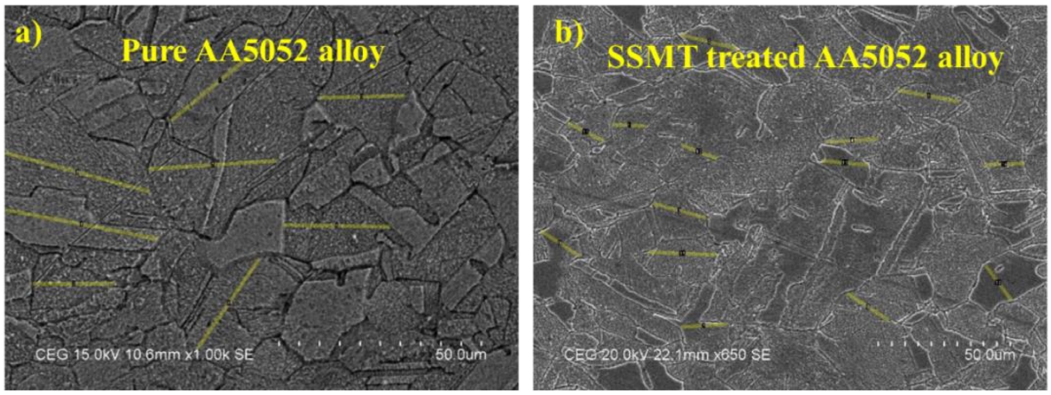

Figure 9. SEM images of (a) untreated AA5052 alloy and (b) optimized SSMT-treated AA5052 alloy

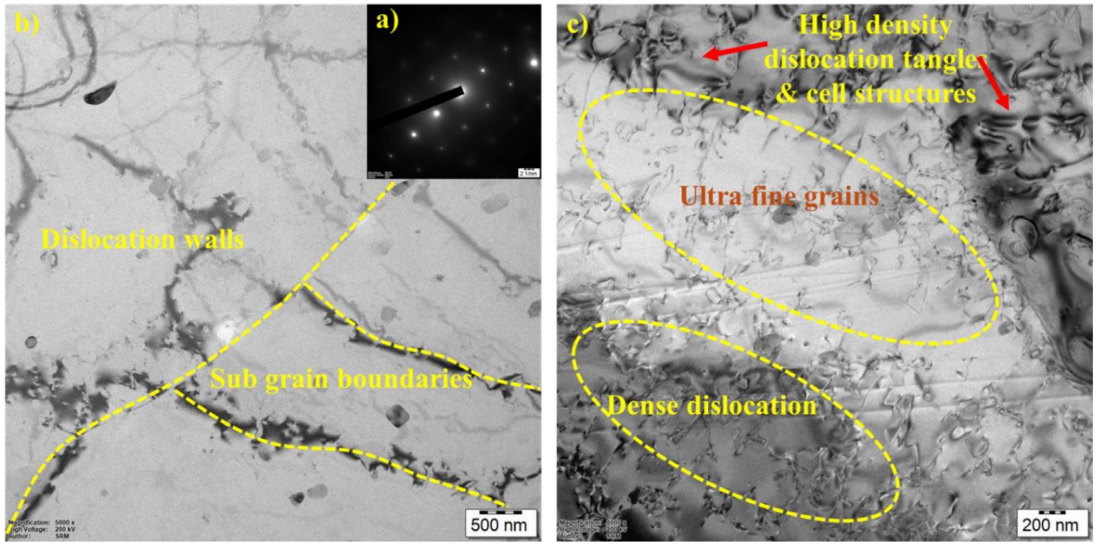

Figure 10. TEM images of a) SEAD pattern, b) & c) optimized SSMT-treated AA5052 alloy

The XRD patterns of the untreated and optimised SSMT-treated AA5052 alloy are depicted in Figure 11(a) and 11(b). The diffraction peaks observed correspond to the FCC phase of aluminum, with dominant reflections indexed to the (111), (200), and (311) planes. For the untreated specimen, the (111) peak appeared sharply with minimal broadening, indicating the presence of coarse grains with relatively low internal strain. In contrast, the optimized SSMT-treated sample exhibited a broadened and slightly shifted (111) peak, signifying significant grain refinement and the generation of compressive residual stresses during treatment.

The crystallite size was calculated using the Debye–Scherrer equation, revealing a substantial reduction from 140.5 nm in the untreated alloy to 40.5 nm in the SSMT-treated alloy. The increased peak broadening observed in the optimized SSMT-treated sample is directly attributed to this refined grain structure.

To further analyze the microstructural strain contribution, the Williamson–Hall (W–H) method was employed, which considers both crystallite size and lattice strain effects on X-ray peak broadening. The W–H relation is expressed as $\beta\cos\theta = (k\lambda/D) + 4\varepsilon\sin\theta$, where β is the full width at half maximum (FWHM) of the diffraction peak (in radians), θ is the Bragg angle, λ is the X-ray wavelength, D is the crystallite size, and ε is the microstrain. A linear plot of $\beta\cos\theta$ versus $4\sin\theta$ was used, where the intercept gives the crystallite size and the slope corresponds to the lattice strain[30].

The calculated microstrain (ε) and dislocation density ($\delta = 1/D^2$) values are summarized in Table 9. The SSMT-treated surface exhibited a microstrain of 8.92×10^{-4} and a dislocation density of 6.10×10^{14} lines/m^2, significantly higher than the untreated sample values of 2.57×10^{-4} and 5.06×10^{13} lines/m^2, respectively. The increase in these parameters confirms that SSMT induces substantial lattice distortion and defect generation due to severe plastic deformation, which enhances the stored energy and contributes to improved hardness and strength. In terms of mechanics, the decrease in crystallite size causes an increase in mechanical strength via the Hall-Petch equation, since the smaller grains produce higher grain boundaries, which can function as effective barriers to dislocation movement, hence increasing the yield strength of the material. Moreover, there is a high dislocation density, which produces dislocation-dislocation interaction leading to strain hardening due to limited dislocation mobility. Increased microstrains represent increased lattice distortions, which create strain fields and prevent slip. On the other hand, severe plastic deformation as a result of SSMT creates compressive residual strains on the surface, which help retard the formation and spread of cracks.

These enhancements are a consequence of the severe surface plastic deformation induced by the SSMT process, which leads to dislocation multiplication and lattice distortion. The formation of nanocrystalline grains and increased dislocation content contribute to the observed peak shift toward higher angles and the FWHM broadening, as clearly shown in the magnified peak of Figure 11(b). These findings show that SSMT treatment effectively modifies the surface crystallographic features of AA5052 alloy, improving its hardness and structural integrity.

The contact angle analysis of the untreated and SSMT-treated AA5052 alloy, presented in Figure 12(a–b), reveals a significant alteration in surface wettability because of surface texturing and microstructural refinement. The untreated AA5052 alloy exhibited contact angles of approximately 73.6° and 72.1°, indicative of a moderately hydrophilic surface. This behavior can be attributed to its relatively smooth morphology and higher surface energy, which promote water spreading and adhesion. The absence of surface irregularities results in uniform wetting, characteristic of metallic surfaces with low roughness and minimal surface deformation.

Following SSMT, the AA5052 alloy displayed a marked increase in contact angle values of 121.9° and 120.2°, reflecting a transition toward hydrophobicity. This enhancement in water repellency stems from the formation of micro- and nano-scale surface asperities created by the repeated impact of steel balls during the peening process. The resultant surface topography increases the real contact area while simultaneously trapping microscopic air pockets, thereby reducing the solid–liquid interfacial energy. According to the Wenzel model, the relationship between the intrinsic contact angle and the apparent contact angle is expressed as $\cos\theta = r\cos\theta$, where r represents the roughness ratio. As $r > 1$ for textured surfaces, the apparent contact angle increases for hydrophobic materials, providing a quantitative explanation for the observed improvement in wetting resistance after SSMT treatment.

The hydrophobic transition observed in the SSMT-treated alloy is also influenced by the combined effects of grain refinement and dislocation-induced surface stress relaxation.

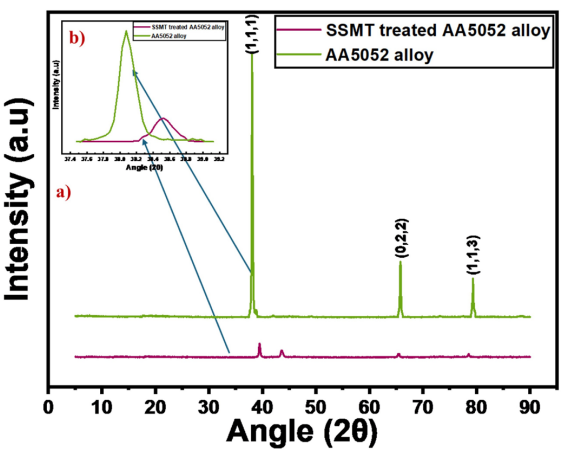

Figure 11. XRD images of (a) Untreated AA5052 alloy and optimized SSMT-treated AA5052 alloy (b) peak shifting and peak broadening analysis.

Table 9. Average grain size, dislocation density, and microstain of AA5052 and optimized SSMT AA5052 alloy.

Parameter	Untreated AA5052	SSMT-Treated AA5052
Grain Size (Dp)	140.5 nm	40.5 nm
Dislocation Density (δ)	5.06×10^{13} lines/m^2	6.10×10^{14} lines/m^2
Microstrain (ε)	2.57×10^{-4}	8.92×10^{-4}

The formation of ultrafine grains and dislocation walls lowers the surface energy by minimizing active adsorption sites and promoting a more stable oxide layer. Moreover, the roughened surface morphology enhances local curvature effects, leading to increased capillary resistance against water spreading. Thus, the synergy between surface roughness, microstructural modification, and surface energy reduction results in a substantial improvement in hydrophobicity. These findings demonstrate that SSMT not only strengthens the mechanical and corrosion properties of AA5052 alloy but also enhances its surface functionality by promoting a self-cleaning, water-repellent character consistent with the Wenzel wetting regime.

3.7. Wear behaviour

The wear test parameters were optimized through preliminary trials to ensure stable wear behavior without excessive material removal. A normal load of 10 N was selected as it represents moderate contact stress sufficient to initiate micro-abrasion while avoiding plastic deformation of the alloy surface. The duration of 20 minutes, corresponding to a sliding distance of approximately 96 m, was chosen based on the point at which the wear rate reached steady-state conditions, indicated by a stable friction coefficient and consistent mass loss between successive intervals. This ensured that the wear mechanisms analyzed reflect true steady-state behavior rather than initial transient effects.

The wear behavior of the untreated AA5052 alloy and the optimized SSMT-treated AA5052 alloy was evaluated using an LRT test under a normal load of 10 N for a duration of 1200 secs. As shown in Figure 13a, the untreated AA5052 exhibited a significantly higher and more fluctuating COF curve, stabilizing at an average of approximately 0.58.

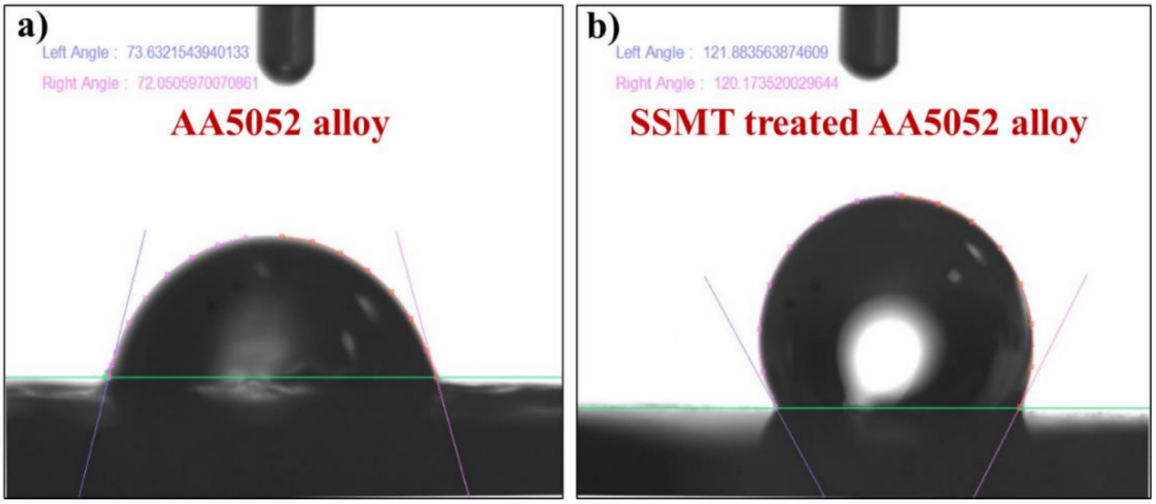

Figure 12. Wettability characteristics of (a) untreated AA5052 alloy and (b) optimized SSMT-treated AA5052 alloy.

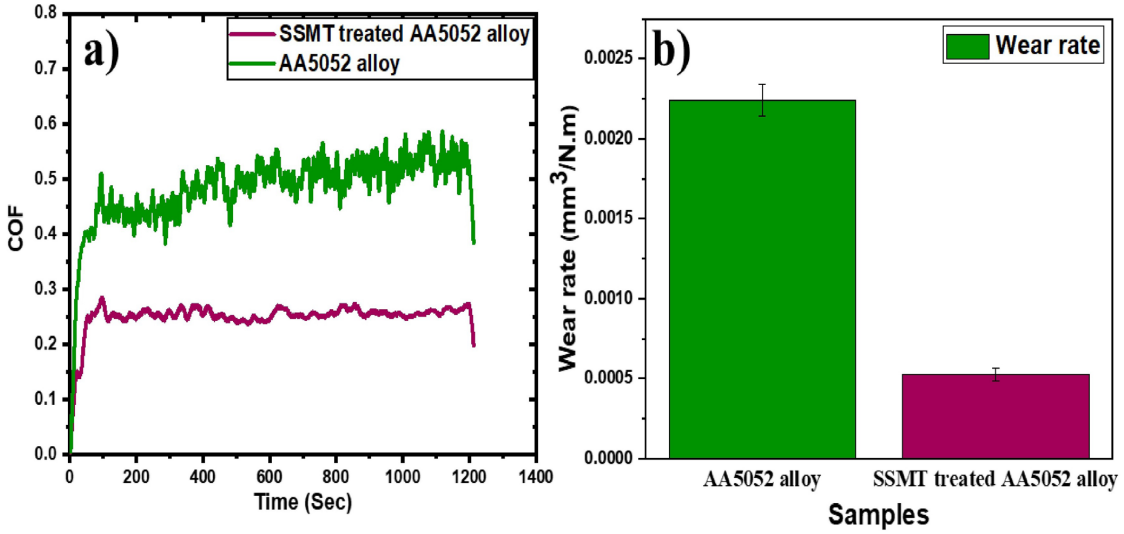

Figure 13. a) COF vs time b) wear rate of AA5052 alloy and SSMT-treated AA5052 alloy.

In contrast, the SSMT-treated specimen demonstrated a markedly reduced and stable COF of around 0.29 throughout the sliding duration. This reduction in frictional resistance can be attributed to the refined surface topography and increased hardness imparted by the SSMT process, which likely minimized adhesion and surface plowing mechanisms.

The specific wear rate was calculated using Archard's law, expressed as K=V/(F×L), where V is the wear volume (m^3), F is the applied normal load (N), and L is the sliding distance (m). The wear volume was determined from the measured mass loss and material density (2.68 g/cm^3). This relation provides a quantitative assessment of the wear resistance improvement achieved through SSMT treatment.

Figure 13b and Table 10 further illustrate the quantitative difference in wear performance between the two samples. The untreated AA5052 alloy incurred a mass loss of 0.00576 g, translating to a volume loss of 2.15 mm^3, while the SSMT-treated alloy experienced a considerably lower mass loss of 0.00135 g, equivalent to a volume loss of 0.504 mm^3. Based on the sliding distance of 96 m, the calculated wear rates were 2.24×10^{-3} $mm^3/N{\cdot}m$ and 5.25×10^{-4} $mm^3/N{\cdot}m$ for the untreated and optimized SSMT-treated samples, respectively. These results indicate a wear rate reduction of approximately 76.5% due to the SSMT treatment. The significant improvement in wear resistance can be attributed to the enhanced surface hardness, grain refinement, and induced compressive residual stresses, which together mitigated material loss during reciprocating sliding.

Figure 14 presents the SEM micrographs depicting the wear surface morphology of both untreated AA5052 alloy (a, b) and optimized SSMT-treated AA5052 alloy (c, d). In the case of the untreated AA5052 alloy, the surface shows a pronounced linear wear track with clearly visible ploughing marks, suggesting severe plastic deformation due to abrasive contact. The presence of wear debris scattered across the track (Figure 14a) indicates material removal via micro-cutting and fragmentation. Moreover, the emergence of distinct adhesive wear zones and debris particles (Figure 14b) points to adhesive interactions between the contact surfaces, leading to localized bonding and tearing.

Table 10. Comparative wear analysis of AA5052 and optimized SSMT AA5052 alloy.

Parameter	AA5052 Alloy	SSMT-Treated AA5052 Alloy
COF	0.58± 0.02	0.29± 0.01
Mass Loss (g)	0.00576± 0.0003	0.00135± 0.0001
Volume Loss (mm^3)	2.15± 0.12	0.504± 0.03
Wear Rate ($mm^3/N{\cdot}m$)	$(2.24 \pm 0.10) \times 10^{-3}$	$(5.25 \pm 0.04) \times 10^{-4}$

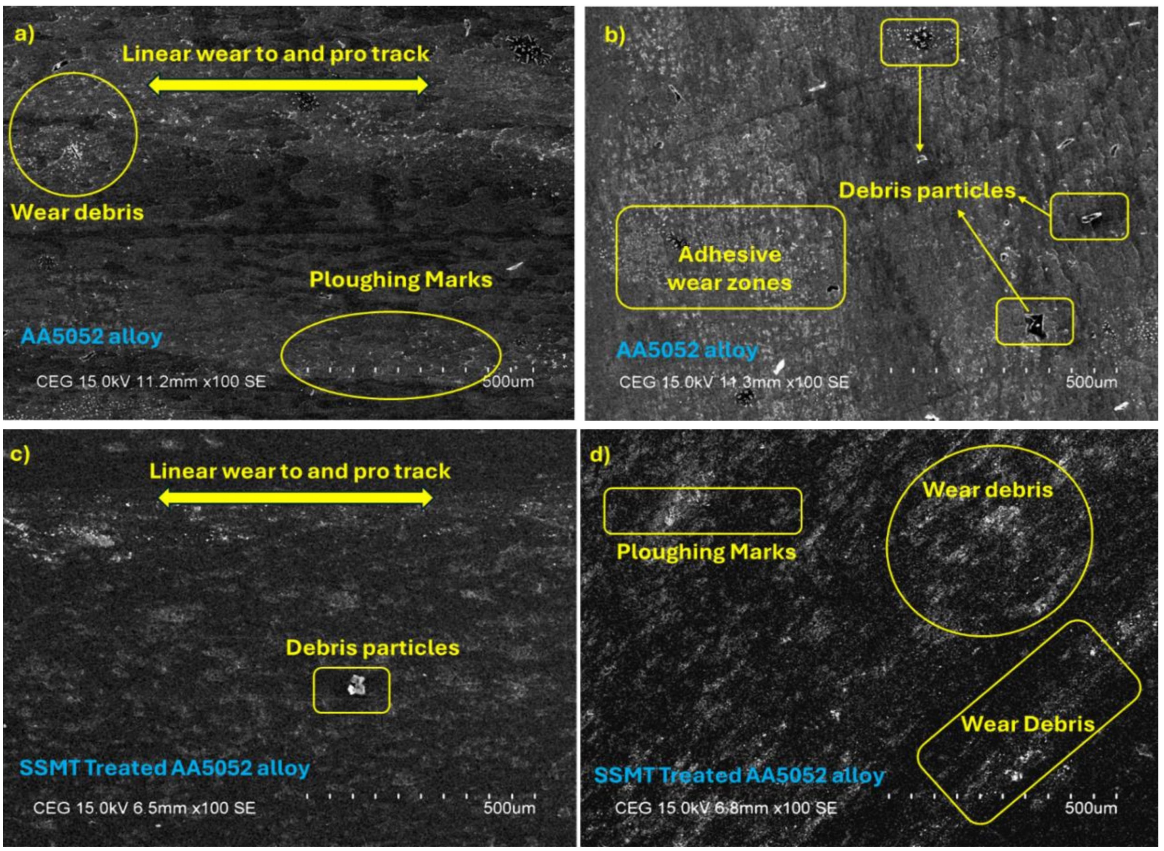

Figure 14. (a,b) wear trace of AA5052 sample, (c,d) optimized SSMT AA5052 sample

Conversely, the SSMT-treated AA5052 alloy surfaces exhibit a more refined wear behaviour. As seen in Figures 14c and 14d, the wear track is comparatively shallow, and although debris particles are still present, their distribution is less extensive, suggesting reduced material degradation. The linear wear path remains visible but appears less aggressive, and ploughing marks are less intense, implying that surface strengthening via SSMT has improved resistance to deformation. The reduced quantity and size of wear debris confirm that the treated alloy endured lower wear severity under identical test conditions. The SEM analysis confirms that the SSMT treatment significantly enhances the wear resistance of AA5052 alloy by minimizing surface damage, reducing debris formation, and limiting adhesive and abrasive wear mechanisms.

3.8. Corrosion behaviour

The electrochemical corrosion analysis presented for both AA5052 alloy and SSMT-treated AA5052 alloy provides a comprehensive understanding of corrosion behavior and surface modification effectiveness under a simulated marine environment. These electrochemical techniques are essential for evaluating the material's response to localized corrosion, pitting susceptibility, and oxide layer stability. During the EIS measurements, an AC perturbation amplitude of 10 mV (rms) was imposed around the open circuit potential (OCP) to maintain linear polarization and ensure precise impedance characterization, as recommended by ASTM G15–19. The OCP profile (Figure 15a) shows that the SSMT-treated alloy stabilizes at a more noble potential compared to the untreated alloy, suggesting delayed initiation of corrosion reactions. However, the OCP value alone cannot fully describe the stability of the surface oxide or hydroxide film; hence, complementary EIS and polarization analyses were conducted to obtain a more reliable evaluation of surface passivation and corrosion resistance.

In the Nyquist plot (Figure 15b), the SSMT-treated AA5052 alloy displays a distinct capacitive loop followed by an inductive loop at low frequencies, whereas the untreated alloy exhibits only a single depressed semicircle. The presence of the inductive loop is associated with adsorption–desorption processes of corrosion intermediates, the dissolution and reprecipitation of corrosion products, and the relaxation of adsorbed species such as Al(OH)ads at the metal–electrolyte interface. The larger inductive loop diameter observed for the SSMT-treated alloy indicates a slower interfacial reaction rate and stronger surface film adherence, suggesting greater resistance to localized pitting initiation. The inductive behavior, therefore, does not directly correspond to higher charge transfer resistance but rather reflects the complex dynamic response of the surface film. The improvement in corrosion resistance is primarily attributed to the combined effects of refined surface grains, increased dislocation density, compressive residual stress, and the formation of a compact, adherent oxide layer that collectively enhances passivation stability. EIS equivalent circuit analysis indicates that the charge transfer resistance (Rct = 3500 $\Omega \cdot cm^2$) of the alloy treated by SSMT is substantially larger than that of the untreated alloy (Rct = 900 $\Omega \cdot cm^2$). At the same time, polarization resistance (Rp = 3200 $\Omega \cdot cm^2$) has also been observed to be increased in the treated alloy (850 $\Omega \cdot cm^2$ in the untreated).

The Bode plot (Figure 15c) further supports these findings. The SSMT-treated alloy exhibits higher impedance magnitudes across the frequency range, particularly in the low-frequency region, which signifies restricted ionic transport through the passive film. The phase angle response shows a broader and higher peak, indicating a more capacitive behavior and a stable passive layer. The observed resistive–inductive transition at low frequencies corresponds to the relaxation of adsorbed intermediates and localized dissolution–reformation of the oxide film, confirming the dynamic stabilization of the surface.

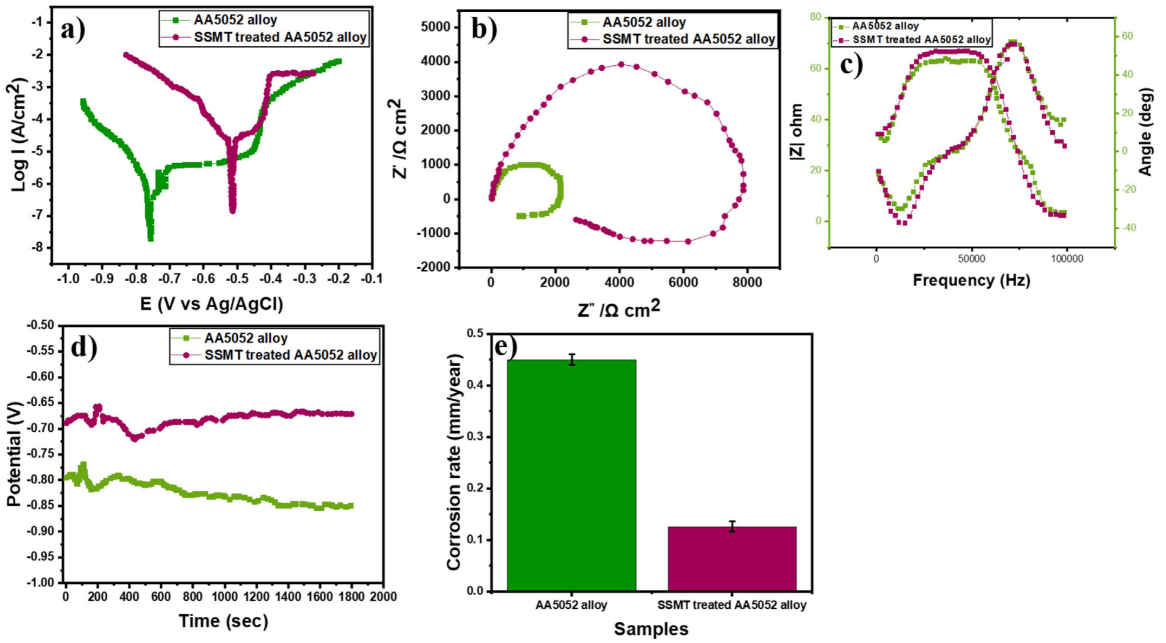

Figure 15. Corrosion analysis of AA5052 alloy and SSMT-treated AA5052 alloy.

In contrast, the untreated AA5052 alloy demonstrates a narrower phase angle peak, signifying an unstable oxide film and enhanced susceptibility to mass loss and pitting attack.

The Tafel polarization curves (Figure 15d) further reveal the influence of SSMT on corrosion behavior. The untreated AA5052 alloy exhibited a corrosion potential (Ecorr) of −0.759 V and a corrosion current density (Icorr) of 4.112×10^{-5} A/cm^2, reflecting higher corrosion activity. The SSMT-treated alloy, however, shifted to a more noble potential (Ecorr = −0.526 V) with a reduced current density (Icorr = 1.153×10^{-5} A/cm^2), indicating improved corrosion resistance. A wider passivation range was also observed for the treated alloy, confirming the formation of a stable and protective passive layer resistant to chloride ion breakdown. The nanostructured surface produced by SSMT facilitates uniform oxide growth and inibits pit initiation, thereby enhancing long-term surface durability and minimizing surface discoloration under corrosive environments. The Rp values obtained from the Tafel plot provide additional evidence that there is indeed a significant increment in the value of Rp from 850 Ω·cm^2 for the treated alloy to 3200 Ω·cm^2 for the SSMT-treated alloy.

To further substantiate these results, both EIS and polarization data were analyzed using equivalent circuit fitting and Tafel extrapolation methods to quantify electrochemical parameters such as charge transfer resistance, double-layer capacitance, and corrosion rate. The combined analysis revealed that the SSMT-treated alloy exhibits superior corrosion resistance owing to the synergistic effect of surface grain refinement, compressive stresses, and defect-minimized passive film formation. The corrosion rate decreased significantly from 0.45 mm/year to 0.126 mm/year (Figure 15e), confirming that SSMT effectively enhances the corrosion performance of AA5052 alloy in chloride-containing environments by improving film stability, delaying pit propagation, and ensuring prolonged passivity retention.

4. Conclusions

The present study demonstrated the significant potential of SSMT in enhancing the surface and mechanical performance of AA5052 aluminium alloy.

- The optimized SSMT process increased the surface microhardness of AA5052 alloy from 130 HV to 193 HV, resulting in a 48.5% improvement. This enhancement is attributed to grain refinement, strain hardening, and the introduction of high dislocation density caused by severe plastic deformation.
- The tensile strength of the alloy improved from 492 MPa to 598 MPa, marking a 21.5% increase. This is primarily due to the formation of ultrafine grains and residual compressive stresses that delay dislocation movement and crack initiation.
- Electrochemical testing in 3.5% NaCl solution showed a significant decrease in corrosion current density (Icorr) from 4.112×10^{-5} A/cm^2 to 1.153×10^{-5} A/cm^2, and corrosion rate reduced from 0.45 mm/year to 0.126 mm/year, indicating a 72% reduction. This improvement is due to the formation of a denser, more stable oxide layer that resists pitting and surface degradation.
- The wear rate dropped from 2.24×10^{-3} mm^3/N·m to 5.25×10^{-4} mm^3/N·m, reflecting a 76.5% improvement. This can be attributed to enhanced surface hardness and smoother energy dissipation during frictional contact due to microstructural changes.
- Contact angle measurements revealed a transformation from moderately hydrophilic behavior (~73°) in the untreated alloy to highly hydrophobic (~121°) after SSMT, driven by the formation of micro-textures and grain refinement on the surface.
- The average grain size was reduced from 140.5 nm to 40.5 nm, a 71% reduction, confirmed by TEM and XRD. The increase in dislocation density and microstrain significantly contributed to improved mechanical integrity and corrosion protection.
- The SSMT-treated samples showed a more positive open circuit potential (OCP), larger Nyquist semicircles, and higher impedance in the Bode plot, confirming superior electrochemical stability and enhanced resistance to localized attack
- The optimized SSMT parameters achieved a closeness coefficient (CC_i) of 0.8976 through TOPSIS analysis, validating the effectiveness of the chosen parameters (6 mm ball diameter, 1000 rpm, 30 minutes) in achieving balanced mechanical and corrosion-resistant properties.

This comprehensive performance improvement highlights the effectiveness of SSMT in significantly enhancing the surface characteristics of AA5052 alloy, making it a viable candidate for applications demanding high strength, corrosion resistance, and wear durability.

5. Data Availability

All data generated or analysed during this study are included in this published article. Additional datasets or supporting information can be made available by the corresponding author upon reasonable request.

6. References

1. Zupanc U, Grum J. Surface integrity of shot peened aluminium alloy 7075-T651. Jixie Gongcheng Xuebao. 2011;57(5):379-84.
2. Huang C, Ye X, Yang X, Yao A, Fan Z. Preparation of a superhydrophobic aluminium alloy surface by UV laser. Surf Eng. 2020;36(6):558-64.
3. Zhao Q, Tang T, Wang F. Fabrication of superhydrophobic AA5052 aluminum alloy surface with improved corrosion resistance and self cleaning property. Coatings. 2018;8(11):390.
4. Achuthankutty A, Saravanan R, Nagarajan H, Pasunuri V, Gopal NH, Ramesh A, et al. Cryo-rolled AA5052 alloy: insights into mechanical properties, formability, and microstructure. Journal of Manufacturing and Materials Processing. 2024;8(6):284.
5. Samal P, Vundavilli PR, Meher A, Mahapatra MM. Influence of TiC on dry sliding wear and mechanical properties of in situ synthesized AA5052 metal matrix composites. J Compos Mater. 2019;53(28-30):4323-36.
6. Shanavas S, Edwin Raja Dhas J, Murugan N. Weldability of marine grade AA 5052 aluminum alloy by underwater friction stir welding. Int J Adv Manuf Technol. 2018;95:4535-46.
7. Lee SH, Jo SH, Jeon JY. Microstructure and mechanical properties of AA6061/AA5052/AA1050 alloy fabricated by cold roll-bonding and subsequently annealed. Korean Journal of Materials Research. 2023;33(11):439-46.

8. Ho KT, Nguyen BH, La NT, Le TS, Pham VT. An experimental study on the tensile strength of friction stir welded AA5052 aluminum alloy. In: Proceeding of 5th International Conference on Advances in Manufacturing and Materials Engineering: ICAMME 2022; 2023 August 9-10; Kuala Lumpur, Malaysia. Proceedings. Singapore: Springer Nature Singapore; 2023. p. 389-95.
9. Sarukasan D, Thirumavalavan K. Influencing laser shock peening treatment of the mechanical, tribological, corrosion, and microstructural characteristics on AA5052 alloy. Surf Eng. 2024;40(9-10):945-66.
10. Mallieswaran K, Rajasekaran S, Vinoth Kumar M, Rajendran C. Steel shot peening effects on friction stir welded AA2014-T6 aluminum alloys. Mater Test. 2022;64(8):1202-13.
11. Sathyajith S, Kalainathan S. Effect of laser shot peening on precipitation hardened aluminum alloy 6061-T6 using low energy laser. Opt Lasers Eng. 2012;50(3):345-8.
12. Dai K, Villegas J, Stone Z, Shaw L. Finite element modeling of the surface roughness of 5052 Al alloy subjected to a surface severe plastic deformation process. Acta Mater. 2004;52(20):5771-82.
13. Xing B, He X, Zeng K, Wang Y. Mechanical properties of self-piercing riveted joints in aluminum alloy 5052. Int J Adv Manuf Technol. 2014;75:351-61.
14. Moradpour M, Khodabakhshi F, Eskandari H. Microstructure–mechanical property relationship in an Al–Mg alloy processed by constrained groove pressing-cross route. Mater Sci Technol. 2018;34(8):1003-17.
15. Abioye TE, Zuhailawati H, Aizad S, Anasyida AS. Geometrical, microstructural and mechanical characterization of pulse laser welded thin sheet 5052-H32 aluminium alloy for aerospace applications. Trans Nonferrous Met Soc China. 2019;29:667-79.
16. Wu J, Djavanroodi F, Gode C, Ebrahimi M, Attarilar S. Microstructure evolution, texture development, and mechanical properties of hot-rolled 5052 aluminum alloy followed by annealing. Mater Res Express. 2022;9(5):056516.
17. Gu J, Zhang X, Yu L. Investigation on anodized 5052 aluminum alloy and its corrosion resistance in simulated acid rain. Int J Electrochem Sci. 2023;18(11):100336.
18. Chen Y, Zhang F. Improving the quality of dissimilar Al/Steel butt-lap joint via ultrasonic-assisted friction stir welding. Materials. 2022;15(5):1741.
19. Gao YK. Improvement of fatigue property in 7050–T7451 aluminum alloy by laser peening and shot peening. Mater Sci Eng A. 2011;528(10-11):3823-8.
20. Benedetti M, Bortolamedi T, Fontanari V, Frendo F. Bending fatigue behaviour of differently shot peened Al 6082 T5 alloy. Int J Fatigue. 2004;26(8):889-97.
21. Asquith DT, Yerokhin AL, Yates JR, Matthews A. Effect of combined shot-peening and PEO treatment on fatigue life of 2024 Al alloy. Thin Solid Films. 2006;515(3):1187-91.
22. Hou H, Dong R, Tan Y, Li C, Zhang X, Wu L, et al. Microstructural characteristics and enhanced mechanical properties of 2024 aluminum alloy resulting from shot-peening treatment. Mater Charact. 2023;206:113412.
23. Hou H, Dong R, Tan Y, Li C, Zhang X, Wu L, et al. Microstructural characteristics and enhanced mechanical properties of 2024 aluminum alloy resulting from shot-peening treatment. Mater Charact. 2023;206:113412.
24. Sarukasan D, Thirumavalavan K. Investigations of surface characteristics on AA5083 alloy with dual treatment. Surf Eng. 2025;41(2):02670844241308369.
25. Unal O, Maleki E. Shot peening optimization with complex decision-making tool: multi criteria decision-making. Measurement. 2018;125:133-41.
26. Thirumavalavan K, Karunamoorthy L, Padmanabhan KA. Mechanical properties of AA6061 aluminium alloy subjected to severe surface mechanical treatment. Mater Res Express. 2019;6(11):1165f6.
27. Parida AK, Routara BC. Multiresponse optimization of process parameters in turning of GFRP using TOPSIS method. Int Sch Res Notices. 2014;2014(1):905828.
28. MatWeb [Internet]. Aluminum 5052-O: ASM material data sheet. Pompano Beach (FL): MatWeb; 2025 [cited 2025 Oct 27]. Available from: https://asm.matweb.com/search/SpecificMaterial.asp?bassnum=MA5052O
29. Gesing TM, Robben L. Determination of the average crystallite size and the crystallite size distribution: the envelope function approach EnvACS. J Appl Cryst. 2024;57(5):1466-76.
30. Achuthankutty A, Saravanan R, Nagarajan H, Pasunuri V, Gopal NH, Ramesh A, et al. Cryo-rolled AA5052 alloy: insights into mechanical properties, formability, and microstructure. Journal of Manufacturing and Materials Processing. 2024;8(6):284.